Universität Karlsruhe (TH)
Forschungsuniversität · gegründet 1825

Institut für Mechanik

Covariant description of contact interfaces considering anisotropy for adhesion and friction Part 2 Linearization, finite element implementation and numerical analysis of the model

Alexander Konyukhov, Karl Schweizerhof
Universität Karlsruhe, Institut für Mechanik

Institut für Mechanik
Kaiserstr. 12, Geb. 20.30
76128 Karlsruhe
Tel.: +49 (0) 721/ 608-2071
Fax: +49 (0) 721/ 608-7990
E-Mail: ifm@uni-karlsruhe.de
www.ifm.uni-karlsruhe.de

Covariant description of contact interfaces considering anisotropy for adhesion and friction Part 2. Linearization, finite element implementation and numerical analysis of the model.

Alexander Konyukhov, Karl Schweizerhof

2006

Abstract.

A covariant description for contact problems including anisotropy for both adhesion and sliding domains is proposed. The principle of maximum dissipation is used to obtain a computational model in the case of quasi-static motions. This second part is first focusing on the linearization of the nonlinear equations necessary for the solution process. Then the finite element implementation for various contact elements is developed. In addition, a mechanical interpretation via a rheological model is discussed. Finally, different cases including curvilinear anisotropy on arbitrary surfaces are considered. The numerical examples are chosen to show the influence of the orthotropy type on the development of the sticking-sliding zone as well as on the kinematical behavior of the contact bodies.

Keywords.
covariant description, anisotropy, contact, adhesion, Coulomb friction, linearization, FE discretization, geometrical isotropy

1 Introduction

In the first part of this contribution contact problems with surfaces possessing anisotropic structure have been formulated via the principle of maximum dissipation in a continuous as well as in an incremental form. The model includes both anisotropy for friction and anisotropy for adhesion. An iterative solution, e.g. of a Newton's type, is required for the solution of the nonlinear contact problem. Thus, we consider in this part the derivation of the necessary consistent tangent matrices for the return-mapping scheme.

The finite implementation of an anisotropic friction law is briefly discussed in Montmitonnet and Hasquin [11] with an application to hot rolling processes, and presented in details in Alart and Heege [1]. A symbolic computation software has been exploited to derive the corresponding tangent matrices in [1]. In the current publication, particular attention is paid to the derivation of tangent matrices in a covariant form allowing the straightforward implementation into a finite element code even for arbitrary curved contact surfaces possessing anisotropic properties for both friction and adhesion.

A rheological model is discussed as a simple mechanical interpretation of the continuous constitutive model. In addition details of finite element implementations for various types of finite element approximations are presented. The set of numerical examples is chosen to show the influence of the orthotropy type on the development of the sticking-sliding zone as well

as on the kinematical behavior of the contact bodies. Thus, constant orthotropy is classified by the eigenvalue ratio of the corresponding tensor defining the adhesion region. These cases are thoroughly investigated by the development of the sticking-sliding zone. It will be shown that a specific combination of both, orthotropy for adhesion and orthotropy for friction, can lead to the so-called geometrical isotropy, when the contact bodies show kinematically isotropic behavior. Finally, it is demonstrated that various kinematical properties of arbitrarily curved contact surfaces can be modeled by means of the adhesion tensor.

2 Consistent linearization for a Newton type solution

The full contact integral can be split into parts for the normal and the tangential directions:

$$\delta W_c = \underbrace{\int_s N \delta\xi^3 ds}_{\delta W_c^N} + \underbrace{\int_s T_j \delta\xi^j ds}_{\delta W_c^T}, \tag{1}$$

therefore, the linearization procedure for a Newton type solution will lead to a normal part and to a tangential part of the tangent matrix. The algorithmic aspects of the linearization include the following operations:

a) linearization of the convective variations, $\delta\xi^i,\ i = 1, 2, 3$

b) linearization of contact traction N and tangential traction T_i taking the return-mapping scheme properly into account.

In order to keep the information as brief as possible, we focus on the specifications for the anisotropic part and refer to previous derivations wherever possible. For the nomenclature we urge the reader to check the first part of the contribution [10].

2.1 Linearization of the variations $\delta\xi^i$

Since the spatial coordinate system is chosen according to the surface geometry, the variational expressions are linearized separately for the tangential variations $\delta\xi^i$, $i = 1, 2$ and for the normal variation $\delta\xi^3$. For details we refer to the derivations already given in [8], [9].

2.1.1 Linearization of the normal variation $\delta\xi^3$

$$\begin{aligned} \frac{d}{dt}\delta\xi^3 \;=\; & -\left(\delta\boldsymbol{\rho}_{,j} \cdot a^{ij}(\mathbf{n}\otimes\boldsymbol{\rho}_i)(\mathbf{v}_\mathrm{s}-\mathbf{v}) + (\delta\mathbf{r}_s - \delta\boldsymbol{\rho})\cdot a^{ij}(\boldsymbol{\rho}_j\otimes\mathbf{n})\mathbf{v}_i\right) \\ & -(\delta\mathbf{r}_s - \delta\boldsymbol{\rho})\cdot h^{ij}(\boldsymbol{\rho}_i\otimes\boldsymbol{\rho}_j)(\mathbf{v}_\mathrm{s}-\mathbf{v})\,. \end{aligned} \tag{2}$$

2.1.2 Linearization of the tangential variations $\delta\xi^i,\ i = 1, 2$

$$\begin{aligned} \frac{d}{dt}\delta\xi^i \;=\; & \\ - \;& \left((\delta\mathbf{r}_\mathrm{s} - \delta\boldsymbol{\rho})\cdot a^{il}a^{jk}\ \boldsymbol{\rho}_k\otimes\boldsymbol{\rho}_l\ \mathbf{v}_j + \delta\boldsymbol{\rho}_j\cdot a^{ik}a^{jl}\ \boldsymbol{\rho}_k\otimes\boldsymbol{\rho}_l\ (\mathbf{v}_\mathrm{s}-\mathbf{v})\right) \\ + \;& (\delta\mathbf{r}_\mathrm{s} - \delta\boldsymbol{\rho})\cdot h^{ij}\left(\boldsymbol{\rho}_j\otimes\mathbf{n} + \mathbf{n}\otimes\boldsymbol{\rho}_j\right)(\mathbf{v}_\mathrm{s}-\mathbf{v}) \\ + \;& h^i_n\dot{\xi}^3\delta\xi^n - \Gamma^i_{kj}\dot{\xi}^j\delta\xi^k. \end{aligned} \tag{3}$$

2.2 Linearization of the contact tractions

The derivative of the normal traction N is written as

$$\dot{N} = -\epsilon_N \dot{\xi}^3. \tag{4}$$

For the linearization of the tangent traction of the reversible part, we recall the evolution equations from Part 1. For the linearization the tangent traction $\mathbf{T}$ has to be considered in the covariant form

$$\frac{d\mathbf{T}}{dt} = \mathbf{B}(\mathbf{v}_\mathrm{s} - \mathbf{v}), \tag{5}$$

leading to the component form in the surface metrics as

$$\frac{\partial T_i}{\partial t} + \nabla_j T_i \dot{\xi}^j = b_{ij}\dot{\xi}^j, \quad j = 1, 2, \tag{6}$$

where the adhesion tensor $\mathbf{B} = b_{ij}\boldsymbol{\rho}^i \otimes \boldsymbol{\rho}^j$ is defined in the surface metrics.

Remark. For a consistent linearization we adopt the assumption that all terms describing the curvature properties of the master surface, i.e. including the second derivatives with respect to convective coordinates, can be neglected based on the numerical investigations in [8] and [9]. This allows to reduce the size of various expressions considerably.

2.3 Linearization of the normal part δW_c^N

According to **Remark 2.2** we write the result given in [8] without the curvature term:

$$D(\delta W_c^N) = \int_s \dot{N}\delta\xi^3 ds + \int_s N\frac{d}{dt}\delta\xi^3 ds$$

$$= -\int_s \epsilon_N(\delta\mathbf{r}_s - \delta\boldsymbol{\rho}) \cdot (\mathbf{n}\otimes\mathbf{n})(\mathbf{v}_s - \mathbf{v}) ds \tag{7}$$

$$-\int_s \epsilon_N \xi^3 \left(\delta\boldsymbol{\rho}_{,j} \cdot a^{ij}(\mathbf{n}\otimes\boldsymbol{\rho}_i)(\mathbf{v}_s - \mathbf{v}) + (\delta\mathbf{r}_s - \delta\boldsymbol{\rho}) \cdot a^{ij}(\boldsymbol{\rho}_j \otimes \mathbf{n})\mathbf{v}_{,i}\right) ds. \tag{7 a}$$

Here, for the first term (the main part) the evolution equation (4) together with the representation of $\delta\xi^3$ by the geometry of the surface is used. For the second term (the rotational part) the regularization for the normal traction together with the linearization of the variation $\delta\xi^3$ in eqn. (2) is taken into account.

2.4 Linearization of the tangential part δW_c^T

The tangential part of the contact integral δW_c^T is considered taking into account the anisotropic evolution equations and the return mapping algorithm. The cases of sticking and sliding have to be treated separately.

2.4.1 The sticking case

Sticking is identified when the trial contact tractions T_i^{tr} computed at load step $(n+1)$ satisfy the conditions imposed by Coulomb's law :

$$\Phi := \sqrt{f^{ij}T_j^{tr}T_i^{tr}} - N < 0. \tag{8}$$

In this case, the real tractions are identical to the trial ones $T_i = T_i^{tr}$, therefore, the linearized traction terms are obtained from the evolution equation in (6) directly. For the convective velocities $\delta\xi^i$, the linearized equations (3) can be used.

$$D_v(\delta W_c^T) = \int_s \left(\frac{dT_i}{dt}\delta\xi^i + T_i \frac{d\delta\xi^i}{dt} \right) ds = \tag{9}$$

in tensor form

$$= \int_s (\delta\mathbf{r}_s - \delta\boldsymbol{\rho}) \cdot \mathbf{B}(\mathbf{v}_s - \mathbf{v}) ds - \tag{9 a\_t}$$

$$- \int_s T_i \left((\delta\mathbf{r}_s - \delta\boldsymbol{\rho}) \cdot a^{il}a^{jk}\ \boldsymbol{\rho}_k \otimes \boldsymbol{\rho}_l\ \mathbf{v}_j + \delta\boldsymbol{\rho}_{,j} \cdot a^{ik}a^{jl}\ \boldsymbol{\rho}_k \otimes \boldsymbol{\rho}_l\ (\mathbf{v}_s - \mathbf{v}) \right) ds, \tag{9 b\_t}$$

or component-wise

$$= \int_s (\delta\mathbf{r}_s - \delta\boldsymbol{\rho}) \cdot b^{ij}\boldsymbol{\rho}_i \otimes \boldsymbol{\rho}_j (\mathbf{v}_s - \mathbf{v}) ds - \tag{9 a\_c}$$

$$- \int_s T_i \left((\delta\mathbf{r}_s - \delta\boldsymbol{\rho}) \cdot a^{il}a^{jk}\ \boldsymbol{\rho}_k \otimes \boldsymbol{\rho}_l\ \mathbf{v}_j + \delta\boldsymbol{\rho}_{,j} \cdot a^{ik}a^{jl}\ \boldsymbol{\rho}_k \otimes \boldsymbol{\rho}_l\ (\mathbf{v}_s - \mathbf{v}) \right) ds. \tag{9 b\_c}$$

The matrices included in this integral obviously preserve symmetry.

2.4.2 The sliding case

The sliding case is identified if the inequality in eqn. (8) is not satisfied. Then the sliding force $\mathbf{T}^{sl}$ is derived from the principle of the maximum dissipation (see Part 1) as

$$\mathbf{T}^{sl} = -\frac{\mathbf{B}\mathbf{F}\mathbf{T}^{tr}}{\sqrt{\mathbf{B}\mathbf{F}\mathbf{T}^{tr} \cdot \mathbf{F}\mathbf{B}\mathbf{F}\mathbf{T}^{tr}}} |N| = -\frac{\hat{\mathbf{T}}|N|}{\Psi}, \tag{10}$$

or component-wise as

$$T_i^{sl} = -\frac{b_{ij}f^{jk}T_k^{tr}}{b_{ij}b_{lm}f^{jk}f^{il}f^{mn}T_k^{tr}T_n^{tr}} \tag{11}$$

In eqn. (10) an auxiliary force $\hat{\mathbf{T}}$ – allowing some reductions in the following expressions – is introduced as

$$\hat{\mathbf{T}} = \mathbf{B}\mathbf{F}\mathbf{T}^{tr}, \tag{12}$$

or component-wise as

$$\hat{T}_i = b_{ij}f^{jk}T_k^{tr} = b_{ij}f_{ln}a^{jl}a^{kn}T_k^{tr} = b_i^j f_j^k T_k^{tr}. \tag{13}$$

and a function Ψ as

$$\Psi := \sqrt{\mathbf{B}\mathbf{F}\mathbf{T}^{tr} \cdot \mathbf{F}\mathbf{B}\mathbf{F}\mathbf{T}^{tr}} = \sqrt{\hat{\mathbf{T}}^{tr} \cdot \mathbf{F}\hat{\mathbf{T}}^{tr}}. \tag{14}$$

The derivative of the sliding force $\mathbf{T}^{sl}$ is computed according to the chain rule as:

$$\begin{aligned} \frac{d\mathbf{T}^{sl}}{dt} = \frac{d}{dt}\left(-\frac{\hat{\mathbf{T}}|N|}{\Psi}\right) &= - \left(\frac{d|N|}{dt}\frac{\hat{\mathbf{T}}}{\Psi} + \frac{|N|}{\Psi}\frac{d\hat{\mathbf{T}}}{dt} - \frac{|N|\hat{\mathbf{T}}}{\Psi^2}\frac{\partial\Psi}{\partial\hat{\mathbf{T}}} \cdot \frac{d\hat{\mathbf{T}}}{dt} \right) \\ &= - \left(\frac{d|N|}{dt}\frac{\hat{\mathbf{T}}}{\Psi} + \frac{|N|}{\Psi}\left[\frac{d\hat{\mathbf{T}}}{dt} - \hat{\mathbf{T}}\frac{\mathbf{F}\hat{\mathbf{T}}}{\Psi^2} \cdot \frac{d\hat{\mathbf{T}}}{dt} \right] \right) \end{aligned} \tag{15}$$

The evolution equation (4) for the normal traction is used for the linearization of $|N|$. The auxiliary force $\hat{\mathbf{T}}$ defined in eqn. (12) is linearized according to the chain rule

$$\frac{d\hat{\mathbf{T}}}{dt} = \frac{\partial \hat{\mathbf{T}}}{\partial \mathbf{T}^{tr}} \frac{d\mathbf{T}^{tr}}{dt} = \mathbf{BFB}(\mathbf{v}^s - \mathbf{v}), \tag{16}$$

where for the linearization of the trial traction $\mathbf{T}^{tr}$ the evolution equation (5) is used directly. It is an interesting fact that due to the tensor representation the linearization is valid even in the case of arbitrarily varying surface tensors $\mathbf{B}$ and $\mathbf{F}$. Eqn. (15) is then transformed into

$$\frac{d\mathbf{T}^{sl}}{dt} = \epsilon_N \dot{\xi}^3 \frac{\hat{\mathbf{T}}}{\Psi} - |N| \left[\frac{\mathbf{BFB}}{\Psi} - \frac{\hat{\mathbf{T}} \otimes (\mathbf{BFB})^T \mathbf{F} \hat{\mathbf{T}}}{\Psi^3} \right] (\mathbf{v}^s - \mathbf{v}). \tag{17}$$

Eqn. (17) is used for the further linearization. After some transformations the following expression in components is obtained for the tangential part of the contact integral

$$D_v(\delta W_c^T) = \int_s \left(\frac{dT_i}{dt} \delta\xi^i + T_i \frac{d\delta\xi^i}{dt} \right) ds = \tag{18}$$

in tensor form denoted by $(\ldots\_t)$

$$= \int_s \left((\delta\mathbf{r}_s - \delta\boldsymbol{\rho}) \cdot \frac{\epsilon_N \hat{\mathbf{T}} \otimes \mathbf{n}}{\Psi} (\mathbf{v}_s - \mathbf{v}) \right) ds \tag{18 a_t}$$

$$- \int_s \left((\delta\mathbf{r}_s - \delta\boldsymbol{\rho}) \cdot \frac{|N| \ \mathbf{BFB}}{\Psi} (\mathbf{v}_s - \mathbf{v}) \right) ds \tag{18 b_t}$$

$$+ \int_s \left((\delta\mathbf{r}_s - \delta\boldsymbol{\rho}) \cdot \frac{|N| \ \hat{\mathbf{T}} \otimes (\mathbf{BFB})^T \mathbf{F} \hat{\mathbf{T}}}{\Psi^3} (\mathbf{v}_s - \mathbf{v}) \right) ds \tag{18 c_t}$$

$$- \int_s T_i^{sl} \left[(\delta\mathbf{r}_s - \delta\boldsymbol{\rho}) \cdot a^{il} a^{jk} \ \boldsymbol{\rho}_k \otimes \boldsymbol{\rho}_l \ \mathbf{v}_j + \delta\boldsymbol{\rho}_{,j} \cdot a^{ik} a^{jl} \ \boldsymbol{\rho}_k \otimes \boldsymbol{\rho}_l \ (\mathbf{v}_s - \mathbf{v}) \right] ds. \tag{18 d_t},$$

or component-wise denoted by $(\ldots\_c)$

$$= \int_s \left((\delta\mathbf{r}_s - \delta\boldsymbol{\rho}) \cdot \frac{\epsilon_N \hat{T}_i a^{ij}}{\Psi} \boldsymbol{\rho}_j \otimes \mathbf{n} (\mathbf{v}_s - \mathbf{v}) \right) ds \tag{18 a_c}$$

$$- \int_s \left((\delta\mathbf{r}_s - \delta\boldsymbol{\rho}) \cdot \frac{|N| \ b_i^k f_j^i b^{jl}}{\Psi} \boldsymbol{\rho}_k \otimes \boldsymbol{\rho}_l (\mathbf{v}_s - \mathbf{v}) \right) ds \tag{18 b_c}$$

$$+ \int_s \left((\delta\mathbf{r}_s - \delta\boldsymbol{\rho}) \cdot \frac{|N| \ b_j^i f_m^j b^{ml} f_i^q \hat{T}_q \hat{T}_n a^{nk}}{\Psi^3} \boldsymbol{\rho}_k \otimes \boldsymbol{\rho}_l (\mathbf{v}_s - \mathbf{v}) \right) ds \tag{18 c_c}$$

$$- \int_s T_i^{sl} \left[(\delta\mathbf{r}_s - \delta\boldsymbol{\rho}) \cdot a^{il} a^{jk} \ \boldsymbol{\rho}_k \otimes \boldsymbol{\rho}_l \ \mathbf{v}_j + \delta\boldsymbol{\rho}_{,j} \cdot a^{ik} a^{jl} \ \boldsymbol{\rho}_k \otimes \boldsymbol{\rho}_l \ (\mathbf{v}_s - \mathbf{v}) \right] ds. \tag{18 d_c}$$

Here, the components of the sliding force T_i^{sl} are computed via eqn. (11), and the components of the auxiliary vector $\hat{T}_i$ via eqn. (13). It becomes obvious, that anisotropy leads to the loss of symmetry of part (18 c_t) and (18 c_c), by looking at the non-diagonal components of $\hat{\mathbf{T}} \otimes \mathbf{A}\hat{\mathbf{T}}$, where

$$\mathbf{A} = (\mathbf{BFB})^T \mathbf{F} \tag{19}$$

then we have

$$\mathbf{C} = \hat{\mathbf{T}} \otimes \mathbf{A}\hat{\mathbf{T}} \implies \left\{ \begin{array}{rcl} c_{12} & = & \hat{T}_1 A_2^1 \hat{T}_1 + \hat{T}_1 A_2^2 \hat{T}_2 \\ c_{21} & = & \hat{T}_2 A_1^1 \hat{T}_1 + \hat{T}_2 A_1^2 \hat{T}_2 \end{array} \right. . \tag{20}$$

Symmetry in eqn. (20) is recovered only in the isotropic case, i.e. if $A_j^i = \delta_j^i$. In the case of isotropy we have $f_j^i = \dfrac{\delta_j^i}{\mu^2}$ and $b_j^i = -\epsilon_T \delta_j^i$ leading to $\Psi = \dfrac{\|\mathbf{T}\|}{\mu^3}$ and $\hat{\mathbf{T}} = -\dfrac{\epsilon_T}{\mu^2} T^{tr}$.

Summarizing we obtain, that the tangent matrix in eqn. (18) consists of the standard constitutive non-symmetric part (18 *a*), a constitutive symmetric part (18 *b*), and a constitutive non-symmetric part (18 *c*), which is symmetric only in the isotropic case, and, finally, the standard symmetric rotational part (18 *d*).

Remark. The component-wise formulas in eqns. (18 *(a, b, c, d)_c*) show the possible representations of the corresponding tensor formulas in eqns. (18 *(a, b, c, d)_t*). It obvious that variations within the sequence of covariant and contravariant components are possible.

3 Finite element implementation.

In this section we will discuss details of the finite element implementation and necessary definitions for the proposed model. In particular, the anisotropic structure has to be defined on the whole contact surface. This leads to additional difficulties concerning a unique description for the whole surface and not only an approximation for the corresponding contact elements. Therefore, we start with the simplest contact element defining contact with an anisotropic rigid surface a so-called a point-to-analytical surface contact element. For this a node of a FE-mesh as well as an integration point of an element can be taken as the contact point. In this case, the contact point itself can be seen as containing history variables. If the anisotropic surface is deformable then the node-to-segment strategy has to be applied. In this case the contact segments store the history variables of passing nodes. As a more general case, the re-parameterization of the complete contact surface in the case of contact of two deformable bodies is discussed.

3.1 Point-to-analytical surface contact element. Linear surface approximation of a deformable body.

The contact of a body meshed with bilinear finite elements – and thus bilinear contact surface elements – with a rigid anisotropic surface is one of the simplest cases to define a contact element. In this case, a node of the FE meshed surface is taken as a contact point, while all necessary anisotropic tensors are defined on the rigid surface which can geometrically be described by analytical functions. The corresponding geometrical characteristics as normal vector $\mathbf{n}$ and tangent vector $\boldsymbol{\rho}_i$ are then directly given by the analytical surface description. All integrals for the tangent matrix as well as for the residuum are defined for one nodal point. Since the anisotropic surface is rigid, all rotational parts can be set to zero. Thus, we obtain the following matrices for the contact contributions.

3.1.1 Matrix for the normal part.

$$\mathbf{K}_N = -\epsilon_N \mathbf{n} \otimes \mathbf{n}. \tag{21}$$

3.1.2 Matrix for the tangential part. Sticking case.

$$\mathbf{K}_T^{stick} = b^{ij}\boldsymbol{\rho}_i \otimes \boldsymbol{\rho}_j. \tag{22}$$

3.1.3 Matrix for the tangential part. Sliding case.

$$\begin{aligned}\mathbf{K}_T^{slide} = \frac{\epsilon_N \hat{T}_i a^{ij}}{\Psi}\boldsymbol{\rho}_j \otimes \mathbf{n} \quad &- \quad \frac{b_i^j f_j^n b_n^l a^{ik}|N|}{\Psi}\boldsymbol{\rho}_k \otimes \boldsymbol{\rho}_l \\ &+ \quad \frac{f_i^q b_j^i f_m^j b^{ml}\hat{T}_q \hat{T}_n a^{nk}|N|}{\Psi^3}\boldsymbol{\rho}_k \otimes \boldsymbol{\rho}_l.\end{aligned} \tag{23}$$

All matrices contain only constitutive parts and belong to the corresponding nodes. The contact node then owns also the necessary history variables from the previous converged step (n): convective coordinates $\xi^1_{(n)}, \xi^2_{(n)}$ and tangential contact forces $T_1^{(n)}, T_2^{(n)}$.

3.2 Point-to-analytical surface contact element. Arbitrary surface approximation of the deformable body.

If a body is meshed with finite elements of higher order of approximation for the surface – leading to a contact element of the same high order – then an integration point of the FE surface elements has to be taken as a contact point. In this case, the vector $\mathbf{r}_s$ describes the analytical surface and the vector $\boldsymbol{\rho}$ is computed from the finite element mesh. Algorithmic aspects of contact problems with a surface described by analytical functions are discussed in [4]. The algorithmic discretization of the tangent matrix, presented in Sect. 2.2, is obtained as follows. Let $\mathbf{u}_e$ be the nodal displacement vector taken from the finite element discretization as

$$\mathbf{u}_e^T = \{u_1^{(1)}, u_2^{(1)}, u_3^{(1)}, u_1^{(2)}, u_2^{(2)}, u_3^{(2)}, ..., u_1^{(n)}, u_2^{(n)}, u_3^{(n)}\}^T, \tag{24}$$

where (n) is a number of nodal points of the contact surface element. Assuming that the approximation is performed with (n) shape functions, only a single position matrix $\mathbf{A}$ is necessary for discretization of all contact contributions.

$$\mathbf{A} = \begin{bmatrix} N_1 & 0 & 0 & N_2 & 0 & 0 & ... & ... & ... & N_{(n)} & 0 & 0 \\ 0 & N_1 & 0 & 0 & N_2 & 0 & ... & ... & ... & 0 & N_{(n)} & 0 \\ 0 & 0 & N_1 & 0 & 0 & N_2 & ... & ... & ... & 0 & 0 & N_{(n)} \end{bmatrix}. \tag{25}$$

The contact matrix for the normal part in eqn. (7) is then obtained as:

$$\begin{aligned}\mathbf{K}_N &= -\int_s \epsilon_N \mathbf{A}^T \mathbf{n} \otimes \mathbf{n}\mathbf{A} ds = \\ &= -\sum_{I,J=1}^{N_p} \left(\epsilon_N \mathbf{A}^T \mathbf{n} \otimes \mathbf{n}\mathbf{A} W_I W_J \det \mathbf{J}(\xi_I^1,\ \xi_J^2)\right),\end{aligned} \tag{26}$$

where N_P is the number of integration points and W_I, $I = 1, 2, ..., N_P$ are weights of the chosen quadrature formula. The determinant of the Jacobian $\det \mathbf{J}(\xi_I^1, \xi_J^2)$ is computed for the surface segment – the contact segment – of the body. For each integration point a set of history variables from the previous converged step (n) must be stored: convective coordinates $\xi^1_{(n)}, \xi^2_{(n)}$ and tangential contact forces $T_1^{(n)}, T_2^{(n)}$. The tangent matrices for the tangential part as defined in Sect. 2.4.1 and 2.4.2 can be derived in similar fashion.

Remark. For this specific case all geometrical characteristics such as normal vector $\mathbf{n}$, tangent vector $\boldsymbol{\rho}_i$ as well as the anisotropic tensors are taken from the rigid surface which is defined by analytical functions.

3.3 Node-to-segment approach. Deformable anisotropic contact surface.

If a deformable body has a surface with anisotropic properties, then the node-to-segment approach can be applied. In this case, the corresponding contact segments covering the anisotropic surface are taken as master segments. A nodal displacement vector contains then an additional $(n+1)$ slave node besides the first (n) nodes from the master segment:

$$\mathbf{u}_e^T = \{u_1^{(1)}, u_2^{(1)}, u_3^{(1)}, ..., u_1^{(n)}, u_2^{(n)}, u_3^{(n)}, u_1^{(n+1)}, u_2^{(n+1)}, u_3^{(n+1)}\}^T. \tag{27}$$

The position matrix $\mathbf{A}$ is modified as

$$\mathbf{A} = \begin{bmatrix} N_1 & 0 & 0 & N_2 & 0 & 0 & ... & N_{(n)} & 0 & 0 & N_{(n+1)} & 0 & 0 \\ 0 & N_1 & 0 & 0 & N_2 & 0 & ... & 0 & N_{(n)} & 0 & 0 & N_{(n+1)} & 0 \\ 0 & 0 & N_1 & 0 & 0 & N_2 & ... & 0 & 0 & N_{(n)} & 0 & 0 & N_{(n+1)} \end{bmatrix}. \tag{28}$$

The components of the tangent matrices (normal and tangent vectors etc.) are computed in the projection point of the master segment. The structure is again algorithmic, e.g. a part for the normal contact has the form:

$$\begin{aligned} \mathbf{K}_N &= -\int_s \epsilon_N \mathbf{A}^T \mathbf{n} \otimes \mathbf{n}\mathbf{A} ds = \\ &= -\epsilon_N \mathbf{A}^T \mathbf{n} \otimes \mathbf{n}\mathbf{A}. \end{aligned} \tag{29}$$

Here, the segment contains the aforementioned history variables.

3.3.1 Mapping of anisotropic properties from the surface to a contact segment.

It is expected, that the anisotropic properties are defined for the complete surface, not only for a segment. Thus, the main problem is, how to properly transfer the anisotropic properties from the surface to the contact segment. In the case of a simple curvilinear rectangular patch this can be organized as follows. Let s^1, s^2 are convective coordinates defining the parameterization of the patch, see Fig. 1, with $0 \leq s^1, s^2 \leq 1$. The anisotropic properties are determined then via the tensor basis $\mathbf{e}_1(s^1, s^2) \otimes \mathbf{e}_2(s^1, s^2)$. The regular numbering $i = 1, ..., m$ and $j = 1, ..., n$ is introduced according to the mapped mesh on the patch, see Fig. 2. Therefore, a direct mapping of the convective coordinate on the element ξ^1 can be defined as

$$\left.\begin{aligned} \xi^1 = -1 \quad &\longrightarrow \quad s^1 = \frac{j-1}{n} \\ \xi^1 = 1 \quad &\longrightarrow \quad s^1 = \frac{j}{n} \end{aligned}\right\} \Longrightarrow s^1 = \frac{2j - 1 + \xi^1}{2n}. \tag{30}$$

According to the introduced direct transformation, the backward transformation is defined

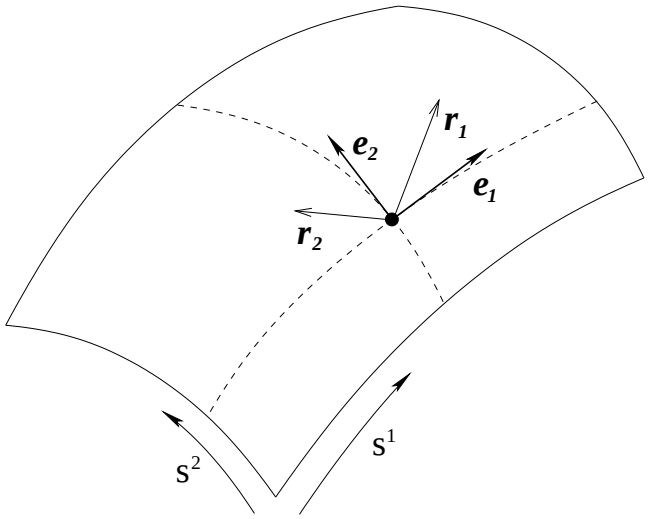

Figure 1: Curvilinear rectangular patch.

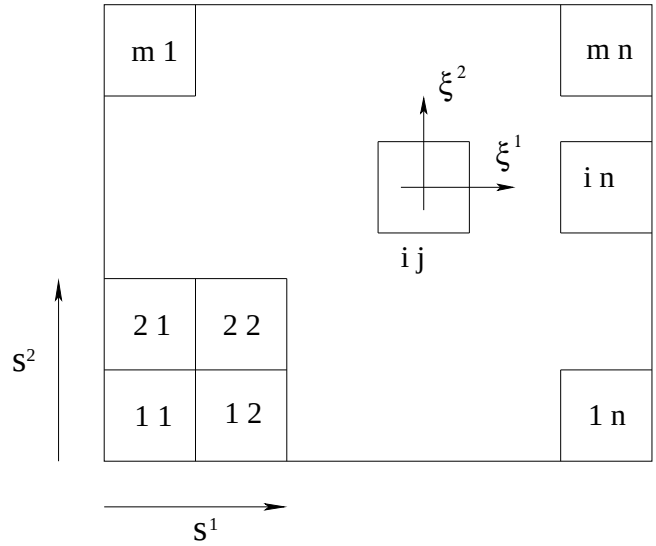

Figure 2: Curvilinear rectangular patch. Mapping scheme.

according to the following algorithm:

$$
\begin{array}{l}
do\ j = 1, n \\
\qquad\qquad if\ \dfrac{j-1}{n} \leq s^1 \leq \dfrac{j}{n} \\
\qquad\qquad then\ k = j \\
\qquad\qquad \xi^1 = 2ns^1 - 2k + 1 \\
\qquad\qquad endif \\
enddo
\end{array}
\tag{31}
$$

The second coordinate s^2 is analogously computed.

4 Numerical examples.

In this section we present numerical examples illustrating several types of the orthotropy. As known, the orthotropic frictional properties of the surface leads to changing of kinematical behavior of the contact bodies, see [2], [3], [5], [7], [14], [15], [16], [17], therefore, the set of numerical examples is chosen to illustrate particular kinematical effects which appear due to presence of anisotropy for adhesion and friction. In the first example we chose constant orthotropy on a plane represented by a tensor with spectral decomposition. This model possesses a simple mechanical interpretation a so-called rheological model. Constant orthotropy is thoroughly investigated for the case with small displacements in order to show the development and the distribution of the sticking-sliding zone for different types of orthotropy. These cases are considered for the start of sliding as well as for large sliding deformations in order to consider the trajectories of a block for different types of orthotropy. Then a large displacement problem for a plane with polar orthotropy is taken as an example for curvilinear orthotropy on the plane. In order to show the robustness of the developed approach for curvilinear surfaces, kinematical effects of a bolt connection are modeled with spiral orthotropy defined on a cylinder.

4.1 Rheological model of the orthotropic adhesion-friction problem.

As is well known [12], the return-mapping scheme used for the model of elasto-plasticity can be interpreted via a one-dimensional spring-sliding system. A generalization of this model into 2D anisotropy is a point on the plane with a two spring-two slider system with different properties: $\varepsilon_1, \varepsilon_2$ as stiffnesses of the springs and μ_1, μ_2 as coefficients of friction for the sliding devices, see Fig. 3. A constant force $\mathbf{F}$ is applied to the point at an angle γ. It becomes obvious, that after transformation of the coordinate system in such a way that e.g. the X-axis coincides with the direction a force $\mathbf{F}$, the problem exactly corresponds to the constant orthotropy on the plane. The latter is given by a tensor with the spectral decomposition in the case of coinciding orthotropy angles for adhesion α and for friction β, see Part 1. The trajectory of the point is then a straight line inclined with an angle φ, the value of which depends on the ratio of the eigenvalues defining the adhesion ellipse, see the geometrical interpretation in Part 1:

$$r_\lambda = \frac{\lambda_1}{\lambda_2} = \frac{\varepsilon_1}{\mu_1} \cdot \frac{\mu_2}{\varepsilon_2} \tag{32}$$

In forthcoming computations, we will show, that it is possible to represent geometrically isotropic behavior, in such a way that the trajectory of the point is coinciding with the direction of the force $\mathbf{F}$, though the properties of this contact surface remain orthotropic.

4.2 Linear constant orthotropy on the plane.

In order to investigate the properties of the proposed model, a rectangular block is considered on an orthotropic plane. The dimensions of the block are $10 \times 10 \times 4$ with linear elastic properties: Young's modulus $E = 2.10 \cdot 10^4$ and Poisson ratio $\nu = 0.3$, assumed within a consistent dimension system. The block (see Fig. 4) is located on the XOY plane and loaded by prescribing displacements on the upper surface in two steps: 1) vertical loading with $w = 1.0 \cdot 10^{-2}$, 2) incremental loading with Δu along the X axis. Contact with regard to the constant orthotropic model with the adhesion tensor

$$\mathbf{B} = [b^i_j] = -\begin{bmatrix} \varepsilon_1 \cos^2\alpha + \varepsilon_2 \sin^2\alpha & (\varepsilon_1 - \varepsilon_2)\sin\alpha\cos\alpha \\ (\varepsilon_1 - \varepsilon_2)\sin\alpha\cos\alpha & \varepsilon_1 \sin^2\alpha + \varepsilon_2 \cos^2\alpha \end{bmatrix}, \tag{33}$$

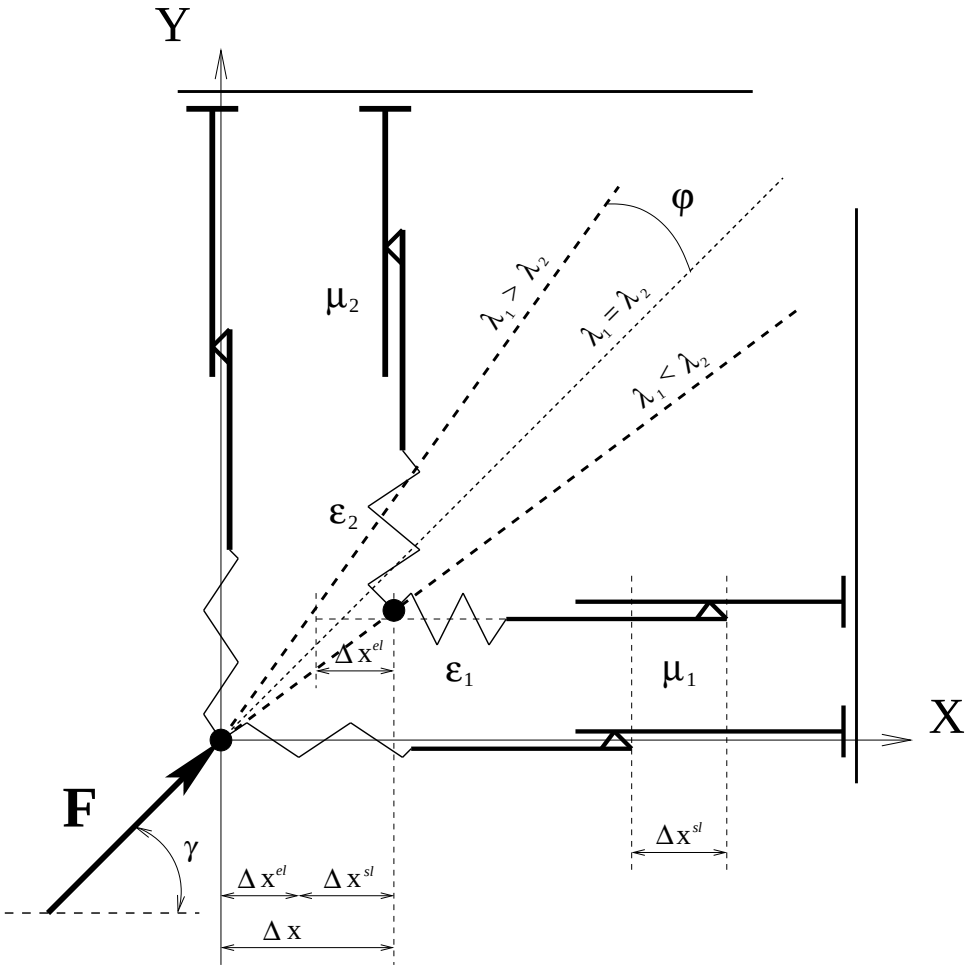

Figure 3: Mechanical interpretation of orthotropic friction – orthotropic adhesion model. A material point on a plane with two spring-slider systems driven by a tangential force.

and the friction tensor

$$\mathbf{F} = [f_k^i] = \begin{bmatrix} \frac{1}{\mu_1^2}\cos^2\beta + \frac{1}{\mu_2^2}\sin^2\beta & (\frac{1}{\mu_1^2} - \frac{1}{\mu_2^2})\sin\beta\cos\beta \\ (\frac{1}{\mu_1^2} - \frac{1}{\mu_2^2})\sin\beta\cos\beta & \frac{1}{\mu_1^2}\sin^2\beta + \frac{1}{\mu_2^2}\cos^2\beta \end{bmatrix} \tag{34}$$

is specified between the plane and the block. To compare both approaches contact is modeled with a point-to-analytical surface contact element as well as with a node-to-segment approach. The rigid plane is taken as master segment within the latter approach. As an example coincident orthotropy angles $\alpha = \beta$ are chosen. First, we will investigate the development of a sticking-sliding zone for small displacements for various cases of the ratio r_λ, see eqn. (32). Afterwards, we will consider the large displacement problem and investigate the trajectories of the block depending on the surface properties.

4.2.1 Small displacement problem. Development of the sticking-sliding zone.

In order to investigate the development of the sticking-sliding zone small displacement increments with $\Delta u = 1.0 \cdot 10^{-4}$ along the X axis are applied. The following cases are considered:

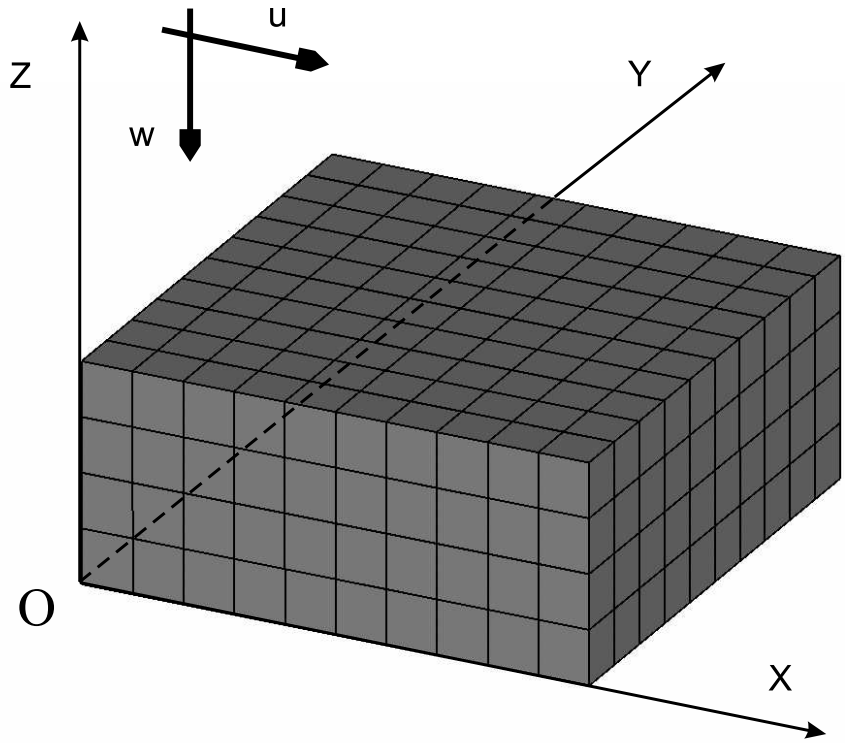

Figure 4: Geometry and loading of the rectangular in plane block.

1. Isotropic case; both, the friction and the adhesion tensors are isotropic with: penalty parameter for the normal traction $\varepsilon_N = 2.1 \cdot 10^5$, parameters of the adhesion tensor $\varepsilon_1 = \varepsilon_2 = 2.1 \cdot 10^5$, parameters of the friction tensor $\mu_1 = \mu_2 = 0.3$. Orthotropy angles: $\alpha = \beta = 0^o$.

2. Geometrically isotropic case with: penalty parameter for the normal traction $\varepsilon_N = 2.1 \cdot 10^5$, parameters of the adhesion tensor $\varepsilon_1 = 3.0 \cdot 10^5$, $\varepsilon_2 = 2.0 \cdot 10^5$, parameters of the friction tensor $\mu_1 = 0.3$, $\mu_2 = 0.2$. Orthotropy angles: $\alpha = \beta = 45^o$. This case leads to the ratio of eigenvalues eqn. (32) $r_\lambda = 1$ and, thus, to a circular adhesion region.

3. Orthotropic case; orthotropic adhesion, isotropic friction with: penalty parameter for the normal traction $\varepsilon_N = 2.1 \cdot 10^5$, parameters of the adhesion tensor $\varepsilon_1 = 2.0 \cdot 10^5$, $\varepsilon_2 = 3.0 \cdot 10^5$, parameters of the friction tensor $\mu_1 = \mu_2 = 0.3$. Orthotropy angles: $\alpha = \beta = 45^o$. The eigenvalue ratio is then $r_\lambda = 2/3$.

4. Orthotropic case; isotropic adhesion, orthotropic friction with: penalty parameter for the normal traction $\varepsilon_N = 2.1 \cdot 10^5$, parameters of the adhesion tensor $\varepsilon_1 = \varepsilon_2 = 2.1 \cdot 10^5$, parameters of the friction tensor $\mu_1 = 0.3$, $\mu_2 = 0.2$. Orthotropy angles: $\alpha = \beta = 45^o$. The eigenvalue ratio is then $r_\lambda = 2/3$.

Isotropic case (1). The results are depicted in the diagram in Figure 6 showing the developed sticking area (in grey color) for the applied horizontal displacements on the lower contact surface in several states from the top view. This area is identified by sticking nodes on the lower contact surface; these nodes are inside the adhesion ellipse. For the results of the investigations we use the node numbering and the inclination angle φ for the block as given in Fig. 5. One can observe that the edge nodes are sliding from the beginning, i.e. when only

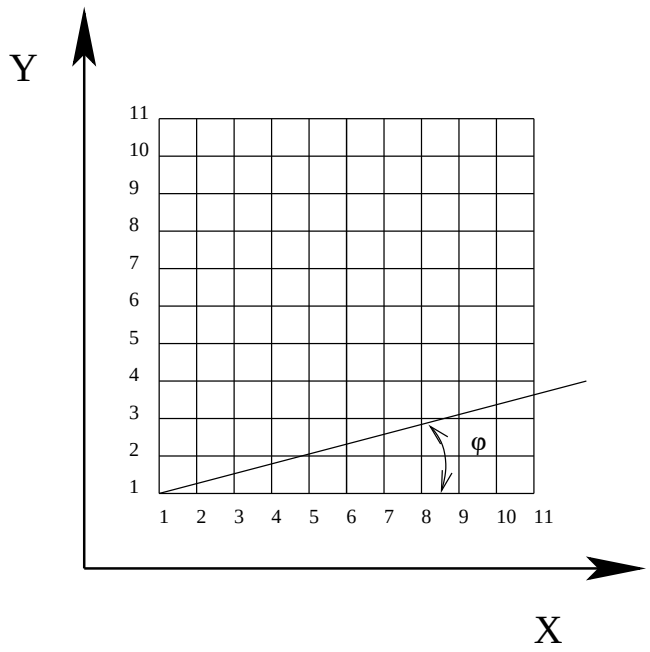

Figure 5: Numbering of nodes on the lower surface and direction φ of the development of a sliding zone.

vertical loading is applied. This effect is due to the singularity of stresses on the edges known from the analytical solution for a rigid punch problem, see e.g. Johnson [6]. The symmetrical sticking region is vanishing and the block begins to slide fully, once the applied horizontal displacements are beyond the value $u = 10.0 \cdot 10^{-3}$.

It is also interesting, especially for the forthcoming orthotropic cases, to observe the beginning of full sliding. Both the initial configuration and the scaled deformed configuration from the bottom view are depicted in Fig. 7 for loading $u = 9.0 \cdot 10^{-3}$ (the block begins to slide partially) as well as for loading $u = 20.0 \cdot 10^{-3}$ (fully developed sliding of the block). The deformation is symmetric as the horizontal axis and the current horizontal symmetry axis are moving along the reference axis.

Geometrically isotropic case (2). The results are depicted in the diagrams in Figure 8 showing the development of the sticking area. It is interesting to observe that the initial sticking area $u = 0.0$ in this case is symmetric along the main orthotropy axes which are turned according to the references coordinate system by the angles $\alpha = \beta = 45^o$.

We recall the geometrical interpretation to explain this phenomena. The adhesion region becomes a circle in this particular example, see Fig. 10. The elastic properties inside the circle are orthotropic according to the computation of the trial force as $\mathbf{T}^{tr} = \mathbf{B}\Delta\mathbf{x}$ with the adhesion tensor computed with $\alpha = 45^o$, see eqn. (33):

$$\mathbf{B} = [b^i_j] = -\frac{1}{2}\begin{bmatrix} \varepsilon_1 + \varepsilon_2 & \varepsilon_1 - \varepsilon_2 \\ \varepsilon_1 - \varepsilon_2 & \varepsilon_1 + \varepsilon_2 \end{bmatrix} = -\frac{10^5}{2}\begin{bmatrix} 5 & 1 \\ 1 & 5 \end{bmatrix}. \tag{35}$$

Since, in the current example the stiffness in the second direction is less then in the first one $\varepsilon_2 < \varepsilon_1$, all points $\mathbf{A}^{el}$ tend to reach the boundary of the adhesion circle in the direction of the ξ^2-axis. This can explain the asymmetric behavior of the initial sticking area in Fig. 8 (a). The direction of the sliding force $\mathbf{T}^{sl}$, which is starting to act from the boundary of the circle, is

defined by the matrix **BFB**, see eqn. (10), which in the current example becomes:

$$\mathbf{BFB} = \frac{1}{2}\begin{bmatrix} \dfrac{\varepsilon_1^2}{\mu_1^2} + \dfrac{\varepsilon_2^2}{\mu_2^2} & \dfrac{\varepsilon_1^2}{\mu_1^2} - \dfrac{\varepsilon_2^2}{\mu_2^2} \\ \dfrac{\varepsilon_1^2}{\mu_1^2} - \dfrac{\varepsilon_2^2}{\mu_2^2} & \dfrac{\varepsilon_1^2}{\mu_1^2} + \dfrac{\varepsilon_2^2}{\mu_2^2} \end{bmatrix} = \begin{bmatrix} 10^6 & 0 \\ 0 & 10^6 \end{bmatrix}. \tag{36}$$

This recovered isotropic behavior of the sliding force $\mathbf{T}^{sl}$ is depicted in Fig. 10. This effect is depicted for the developed sliding in Fig. 9, where the horizontal axis of symmetry of the deformed body is moving along the reference axis.

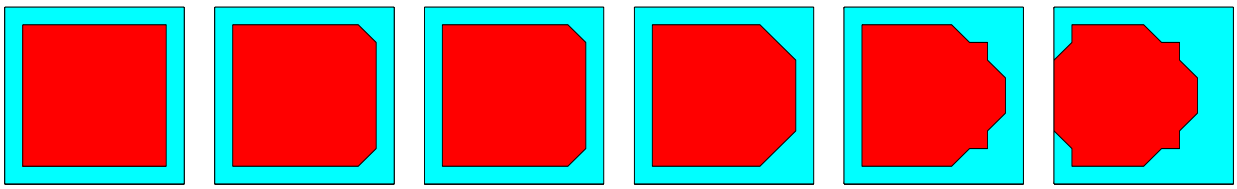

(a) $u = 0.0$ (b) $u = 1.0$ (c) $u = 2.0$ (d) $u = 3.0$ (e) $u = 4.0$ (f) $u = 5.0$

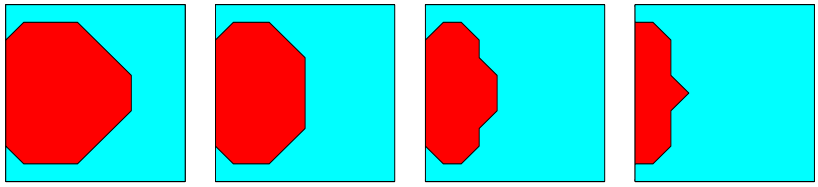

(g) $u = 6.0$ (h) $u = 7.0$ (i) $u = 8.0$ (j) $u = 9.0$

Figure 6: Isotropic case (1). Development (degeneration) of sticking zone for several displacement states. Horizontally applied displacement u pointing into the right direction (u is scaled by 10^{-3}).

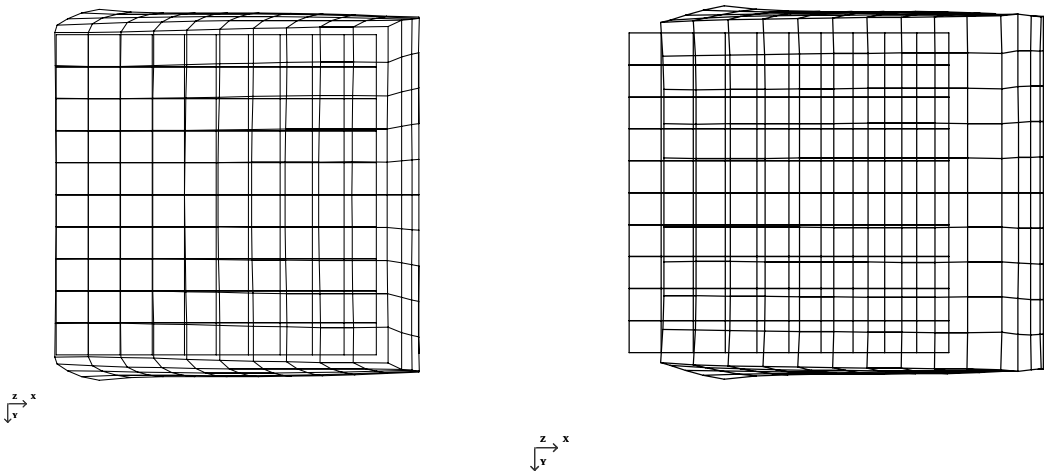

(a) (b)

Figure 7: Isotropic case (1). Deformed and initial configuration. Bottom view. Displacements scaled by factor 150. Applied horizontal displacements on the upper surface: (a) $u = 9.0 \cdot 10^{-3}$ (start of sliding); (b) $u = 20.0 \cdot 10^{-3}$ (fully developed sliding).

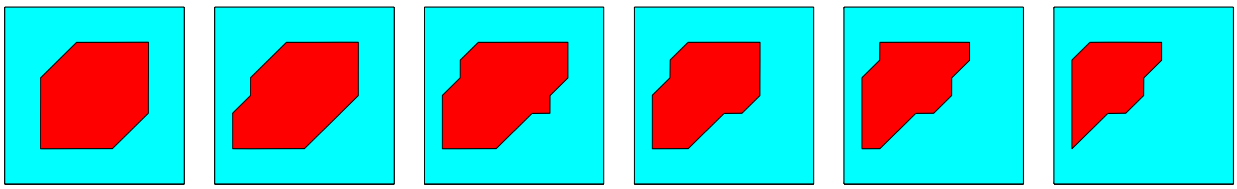

(a) $u = 0.0$ (b) $u = 1.0$ (c) $u = 2.0$ (d) $u = 3.0$ (e) $u = 4.0$ (f) $u = 5.0$

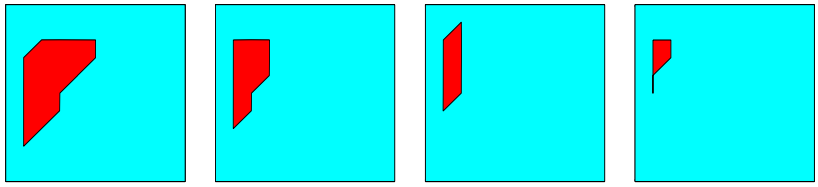

(g) $u = 6.0$ (h) $u = 7.0$ (i) $u = 8.0$ (j) $u = 9.0$

Figure 8: Geometrically isotropic case (2). Development of the sticking zone for various displacement states. Horizontally applied displacement u pointing into the right direction (u is scaled by 10^{-3}).

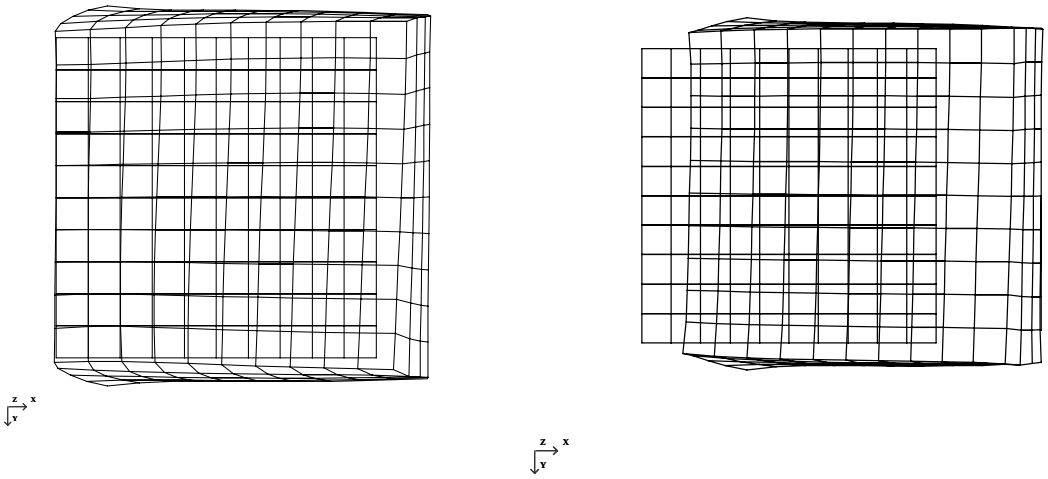

(a) (b)

Figure 9: Geometrically isotropic case (2). Deformed and initial configuration. Bottom view. Displacements scaled by factor 150. Applied horizontal displacements on the upper surface: (a) $u = 9.0 \cdot 10^{-3}$ (start of sliding); (b) $u = 20.0 \cdot 10^{-3}$ (fully developed sliding).

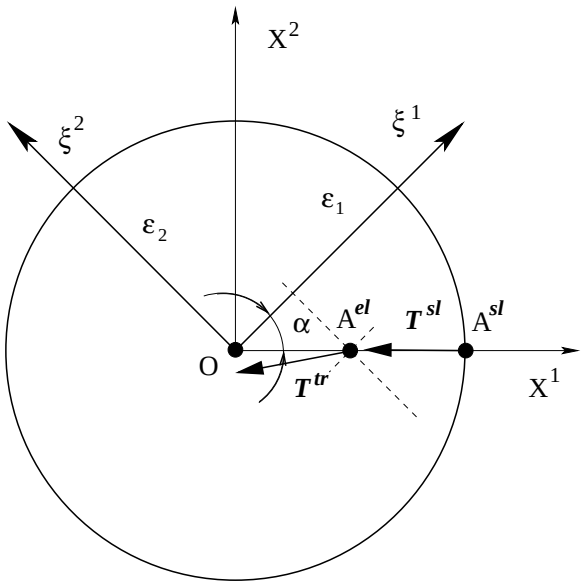

Figure 10: Adhesion region and direction of an elastic trial force and a sliding force for specially chosen parameters leading to the geometrically isotropic case (2). $\varepsilon_1 < \varepsilon_2$, $\alpha = 45^o$.

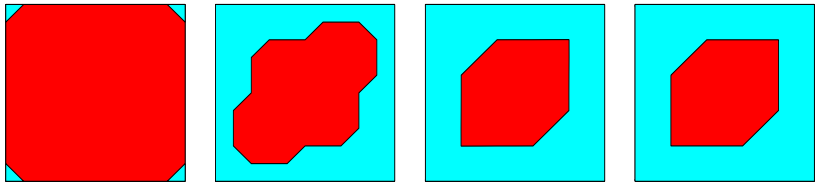

(a) 10^3 (b) 10^4 (c) 10^5 (d) 10^6

Figure 11: Geometrically isotropic case (2). Initial sticking zone. Variation of penalty and adhesion tensor parameters. (a) scale factor 10^3, one load step. (b) scale factor 10^4, one load step. (c) scale factor 10^5, one load step. (d) scale factor 10^6, 10 load steps.

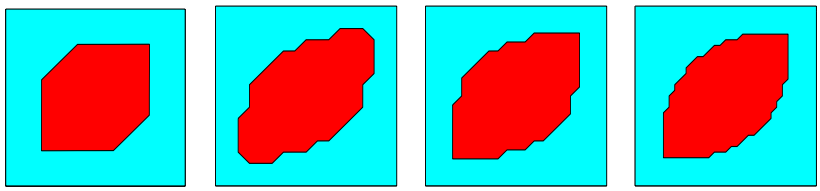

(a) 10×10 (b) 16×16 (c) 20×20 (d) 32×32

Figure 12: Geometrically isotropic case (2). Initial sticking zone. Variation of mesh density. (a) 10×10 elements in plane. (b) 16×16 elements in plane. (c) 20×20 elements in plane. (d) 32×32 elements in plane.

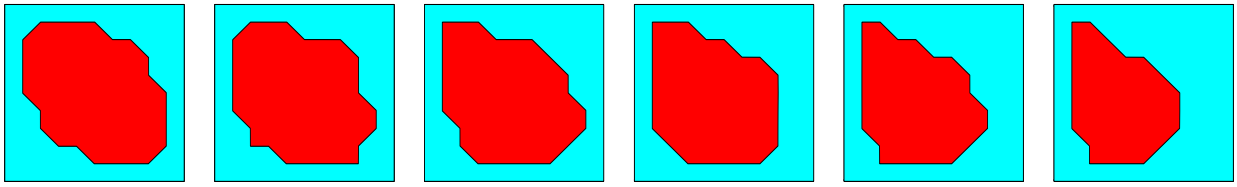

(a) $u = 0.0$ (b) $u = 1.0$ (c) $u = 2.0$ (d) $u = 3.0$ (e) $u = 4.0$ (f) $u = 5.0$

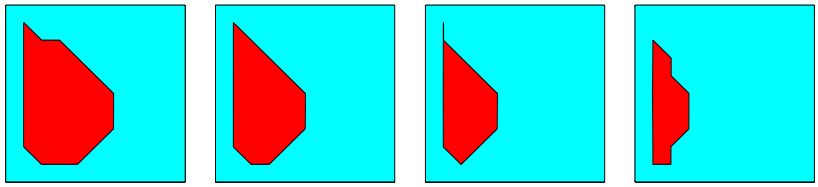

(g) $u = 6.0$ (h) $u = 7.0$ (i) $u = 8.0$ (j) $u = 9.0$

Figure 13: Orthotropic case (3). Development (degeneration) of sticking zone for several displacement states. Horizontally applied displacement u pointing into the right direction (u is scaled by 10^{-3}).

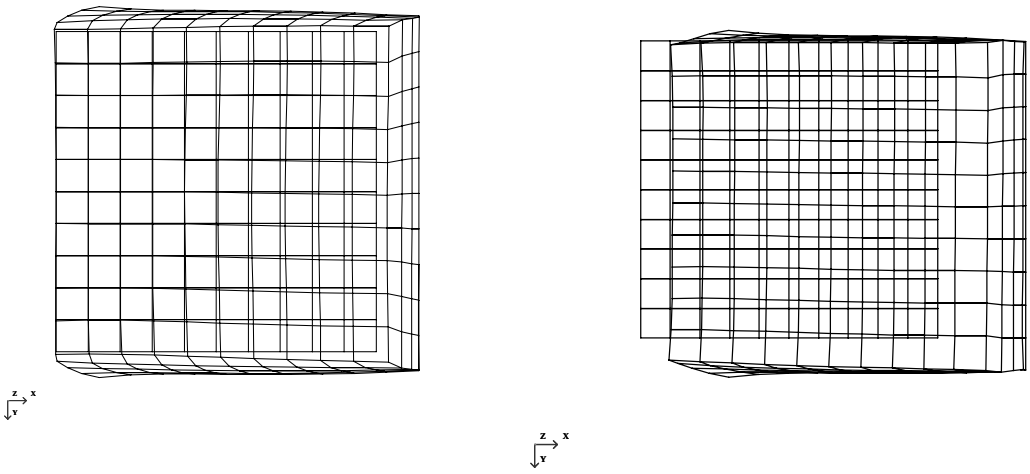

(a) (b)

Figure 14: Orthotropic case (3). Deformed and undeformed configuration. Bottom view. Displacements scaled by factor 150. Applied horizontal displacements on the upper surface: (a) $u = 9.0 \cdot 10^{-3}$ (start of sliding); (b) $u = 20.0 \cdot 10^{-3}$ (fully developed sliding).

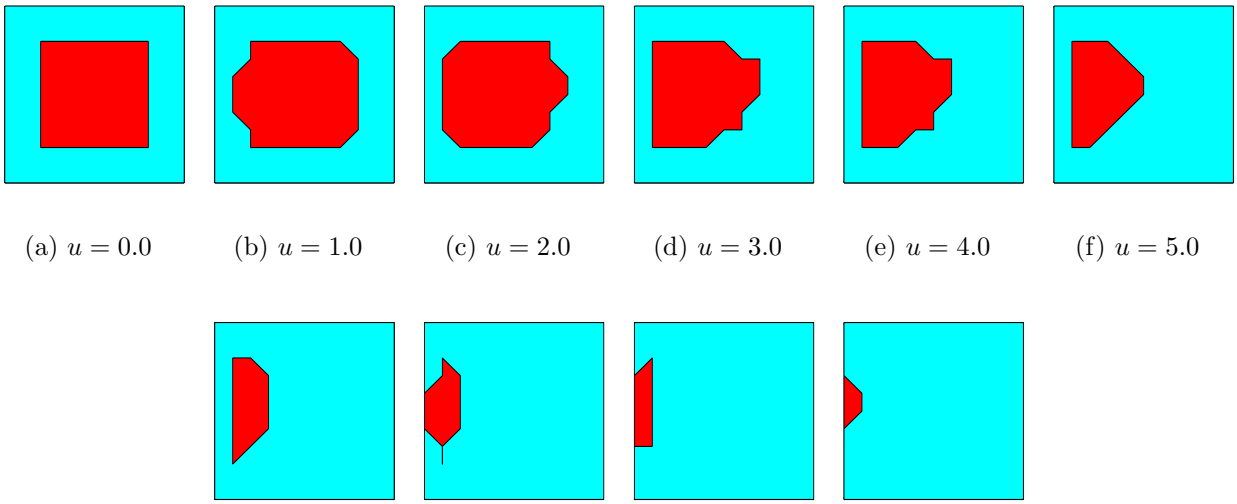

(a) $u = 0.0$ (b) $u = 1.0$ (c) $u = 2.0$ (d) $u = 3.0$ (e) $u = 4.0$ (f) $u = 5.0$

(g) $u = 6.0$ (h) $u = 7.0$ (i) $u = 8.0$ (j) $u = 9.0$

Figure 15: Orthotropic case(4). Development (degeneration) of sticking zone for several displacement states. Horizontally applied displacement u pointing into the right direction (u is scaled by 10^{-3}).

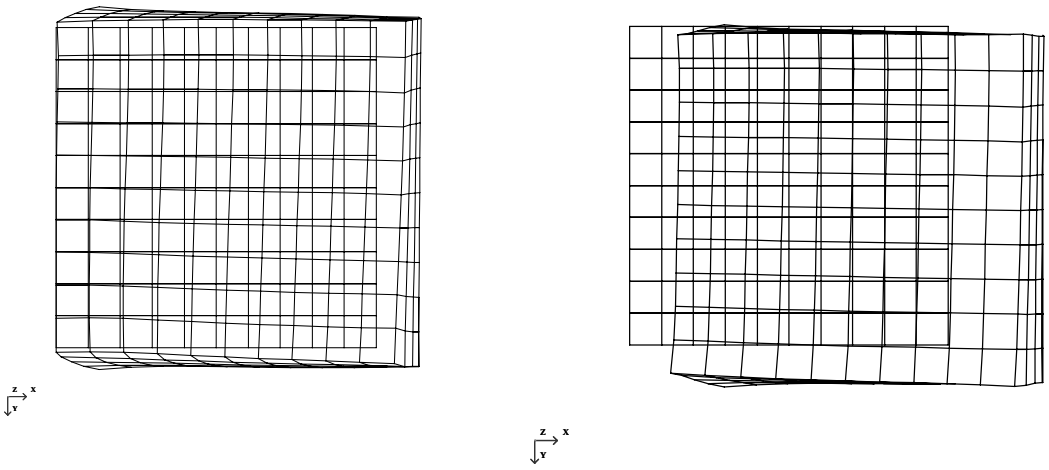

(a) (b)

Figure 16: Orthotropic case (4). Deformed and undeformed configuration. Bottom view. Displacements scaled by factor 150. Applied horizontal displacements on the upper surface: (a) $u = 9.0 \cdot 10^{-3}$ (start of sliding); (b) $u = 20.0 \cdot 10^{-3}$ (fully developed sliding).

For completeness, we would like to present the results showing the convergence of the sticking zone with regard to: 1) adhesion parameters; 2) mesh density. Thus, Fig. 11 represents the comparison of the initial sticking zones computed first for the set of parameters $\varepsilon_N = 2.1 \cdot 10^3$, $\varepsilon_1 = 3.0 \cdot 10^3$, $\varepsilon_2 = 2.0 \cdot 10^3$, then for the same set, but instead of 10^3 scaled sequentially by the factors 10^4, 10^5 and 10^6. For the latter computation the vertical loading has been provided in 10 load steps. The results serve also to show the convergence of the results with increasing penalty parameters.

The influence of the mesh density on the sticking zone for the case of parameters $\varepsilon_N = 2.1 \cdot 10^5$, $\varepsilon_1 = 3.0 \cdot 10^5$, $\varepsilon_2 = 2.0 \cdot 10^5$ is shown in Fig. 12. The uniform mesh was varied as $10 \times 10 \times 4$, $16 \times 16 \times 6$, $20 \times 20 \times 8$ and $32 \times 32 \times 8$ respectively, the third number always representing the number of elements in thickness direction.

Orthotropic case (3). The results are depicted in the diagrams in Fig. 13 showing the development of a closed sticking area. The orthotropy of the adhesion region results in the sticking region being turned by the angle 45^o. The development of a sliding zone starts at the upper right corner and continues unsymmetrically leading further to a parallel shifting of the block and a straight trajectory inclined at an angle φ (see definition at Fig. 5) in the case of large displacements. This effect is depicted in Fig. 14, a bottom view.

Orthotropic case (4). The results are depicted in the diagrams in Fig. 15 showing the development of a closed sticking area. Now, isotropy for the adhesion region together with a small difference between the friction coefficients results in the obtained symmetric region. As known, large differences between the coefficients lead to an unsymmetrical region, see e.g. the results for the classical orthotropic friction model in [5]. The sticking region is diminishing unsymmetrically resulting globally in a shifting of the block, see Fig. 16.

4.2.2 Large displacement problem. Investigation on influence of adhesion parameters on the trajectory of the block.

The goal of this analysis is to show that with properly chosen parameters for the adhesion tensor it is possible to achieve a predefined motion on the surface. Namely, if the surface is uniformly orthotropic with a given orthotropy angle α then it is possible to prescribe a straight trajectory of the block with an angle $\varphi \approx \alpha$, see Fig. 5, keeping the driving force at a certain level. Moreover, it is possible to obtain even the geometrically isotropic case, when a trajectory is a straight line coinciding with the direction of the force, though the friction tensor remains orthotropic leading to different global forces in the different global directions.

In the numerical examples the penalty parameter for the normal traction is kept to $\varepsilon_N = 2.1 \cdot 10^4$ for all cases; the orthotropy angles are given as $\alpha = \beta = 45^o$. The horizontal incremental displacements are taken as $\Delta u = 5.0 \cdot 10^{-2}$ in order to reach a sliding state of the block from the beginning. The other parameters are varied to achieve different cases as presented in Table 1.

Case	Adhesion tensor	Friction tensor	Eigenvalue ratio	Resulting angle φ
1	$\varepsilon_1 = 3.0 \cdot 10^3$ $\varepsilon_2 = 0.0$	$\mu_1 = \mu_2 = 0.3$	∞	-44.95^o
2	$\varepsilon_1 = 3.0 \cdot 10^3$ $\varepsilon_2 = 2.0 \cdot 10^3$	$\mu_1 = \mu_2 = 0.3$	$3/2$	-21.01^o
3	$\varepsilon_1 = 3.0 \cdot 10^3$ $\varepsilon_2 = 2.0 \cdot 10^3$	$\mu_1 = 0.3$ $\mu_2 = 0.2$	1 geom. isotropy	0^o
4	$\varepsilon_1 = 2.0 \cdot 10^3$ $\varepsilon_2 = 3.0 \cdot 10^3$	$\mu_1 = \mu_2 = 0.3$	$2/3$	21.01^o
5	$\varepsilon_1 = 0.0$ $\varepsilon_2 = 3.0 \cdot 10^3$	$\mu_1 = \mu_2 = 0.3$	0	44.95^o

Table 1: Sliding of a block on a plane. Large displacement problem. Variation of orthotropy. Computed inclination angle of a sliding block φ.

The trajectories of the block for all cases are depicted in Fig. 17. It becomes obvious that the block tends to move into the direction of the eigenvector with smaller eigenvalue λ. E.g. if $r_\lambda = \varepsilon_1/\varepsilon_2 = 0$, then the trajectory is inclined at the angle of orthotropy $\varphi \approx \alpha = 45^o$ and vice versa if $r_\lambda = \varepsilon_1/\varepsilon_2 = \infty$, i.e. $\varepsilon_2 = 0$, then the block is inclined at angle $\varphi \approx -45^o$. The other parameter variations lead to different trajectories with angles $-45^o < \varphi < 45^o$. As a particular example, the geometrically isotropic case is recovered for the ratio $r_\lambda = 1$ leading to a circular adhesion region. In this particular case the block is moving into the direction of the applied force.

4.3 Polar orthotropy on a plane. Large displacement problem.

A more complex orthotropy is given by a polar orthotropy on a plane, see Part 1. As in the previous example, we will show that it is possible to define the orthotropic structure of a plane by using the adhesion tensor. An elastic block with dimensions $1 \times 1 \times 0.25$ and mesh $4 \times 4 \times 1$ is sitting on a rigid block, see Fig. 18. Linear elastic material is assumed within a consistent dimension system: Young's modulus $E = 2.10 \cdot 10^4$; Poisson ratio $\nu = 0.3$. The loading is applied sequentially by prescribing displacements on the upper surface in $(1 + n)$ steps: 1) vertical loading with $w = 1.0 \cdot 10^{-2}$, 2) n steps with horizontal displacement increments

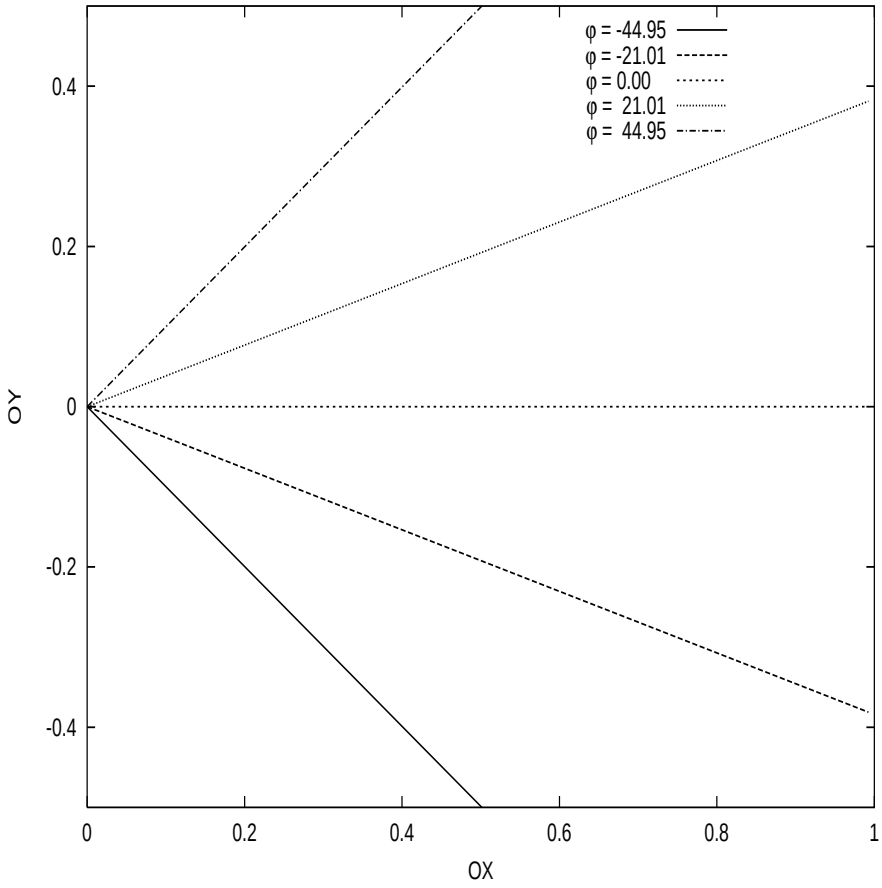

Figure 17: Trajectories of the block and inclination angle φ for various cases of orthotropy with the eigenvalue ratios: $r_\lambda = \infty \Longrightarrow \varphi = -44.95^o$; $r_\lambda = 3/2 \Longrightarrow \varphi = -21.01^o$; $r_\lambda = 1.0 \Longrightarrow \varphi = 0.00^o$; $r_\lambda = 2/3 \Longrightarrow \varphi = 21.01^o$; $r_\lambda = 0.0 \Longrightarrow \varphi = 44.95^o$.

$\Delta u = 1.0 \cdot 10^{-2}$ along the X axis. The structure of the adhesion tensor is as follows, see the derivation in Part 1:

$$\mathbf{B} = -\frac{1}{x^2+y^2}\begin{bmatrix} \varepsilon_r x^2 + \varepsilon_\varphi y^2 & (\varepsilon_r - \varepsilon_\varphi)xy \\ (\varepsilon_r - \varepsilon_\varphi)xy & \varepsilon_r y^2 + \varepsilon_\varphi x^2 \end{bmatrix}. \tag{37}$$

The chosen contact surface parameters are: penalty parameter for the normal traction $\varepsilon_N = 2.1 \cdot 10^5$; isotropic friction tensor with $\mu_1 = \mu_2 = 0.2$. Adhesion tensor with cases: a) $\varepsilon_r = 100$, $\varepsilon_\varphi = 1000$, b) $\varepsilon_r = 2000$, $\varepsilon_\varphi = 5000$, c) $\varepsilon_r = 1000$, $\varepsilon_\varphi = 1000$, d) $\varepsilon_r = 5000$, $\varepsilon_\varphi = 2000$, e) $\varepsilon_r = 1000$, $\varepsilon_\varphi = 100$, f) $\varepsilon_r = 1000$, $\varepsilon_\varphi = 0.0$.

In Fig. 19 the sequence of the motions for all cases leading to different ratios $r_\varepsilon = \varepsilon_\varphi/\varepsilon_r$ is depicted. It is obvious, that the desired circular motion can be achieved by prescribing the corresponding eigenvalue to a small value, e.g. $r_\varepsilon = 0.0$ in the current example. The last result can be derived also analytically from the analysis of global motion of a block, see proof in **Appendix**.

Remark. The trajectory of the block depends on the ratio $\lambda_\varphi/\lambda_r$. However, the numerical computations show that it is possible to prescribe the desired trajectory by only controlling the adhesion tensor parameters. Attempts to achieve the desired trajectory controlling the friction tensor parameters, e.g. taking $\mu_r \approx 0$ for the case (f), lead to disconvergence. A

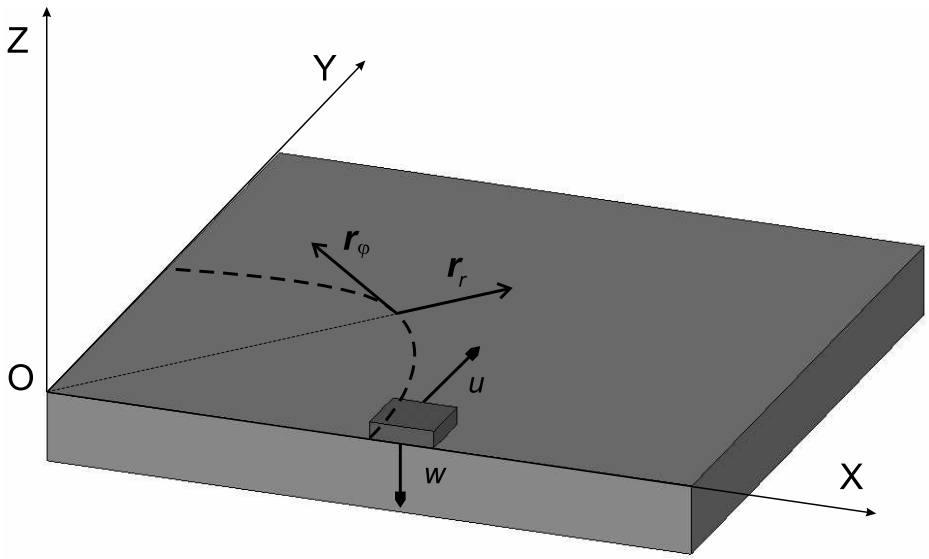

Figure 18: Geometry and loading for the case of polar orthotropy.

straightforward conclusion is that the geometrical structure of the surface in the sense of the desired trajectory can be defined via the adhesion tensor, while other mechanical characteristics such as the measured global forces are defined via the friction tensor.

4.4 Spiral orthotropy on the cylinder.

Another rather complex kinematical behavior of a curved contact surface, e.g. a machined surface of a bolt can be described by means of controlling the adhesion tensor parameters. The model of spiral orthotropy on the cylinder developed in Part 1 allows to describe the kinematical behavior of a bolt connection with a rather coarse mesh. In order to show this, we consider a finite element model of the bolt, see Fig. 20.

The bolt is modeled with linear finite elements with elastic properties: $E = 2.1 \cdot 10^4$, $\nu = 0.3$. Contact is modeled with the point-to-analytical surface contact element and specified on the cylindrical surface of the bolt, i.e. each node on the bolt surface is a contact node. The important dimensions of the example are the radius of a cylinder $R = 3.0$ and the distance H between threads of a spiral line $H = 3.3333$. The central axis is constrained to move along the OZ-axis and a rotation with an angle increment $\Delta\varphi = 1^o$ is applied to the head of the bolt. In order to supply contact with a rigid external cylindrical surface an initial penetration is specified as $1.0 \cdot 10^{-4}$ with a normal penalty parameter $\varepsilon_N = 10^3$. The friction tensor is chosen to be isotropic with $\mu_1 = \mu_2 = 0.01$. The adhesion tensor parameters $\varepsilon_1, \varepsilon_2$ are chosen according to the following tensor representation (see derivation in Part 1)

$$\mathbf{B} = b_{ij}\boldsymbol{\rho}^i \otimes \boldsymbol{\rho}^j = -\frac{1}{R^2 + \left(\dfrac{H}{2\pi}\right)^2} \begin{bmatrix} g_\varepsilon R^2 & (\varepsilon_1 - \varepsilon_2)\dfrac{R^2 H}{2\pi} \\ (\varepsilon_1 - \varepsilon_2)\dfrac{R^2 H}{2\pi} & \varepsilon_1 \left(\dfrac{H}{2\pi}\right)^2 + \varepsilon_2 R^2 \end{bmatrix} \tag{38}$$

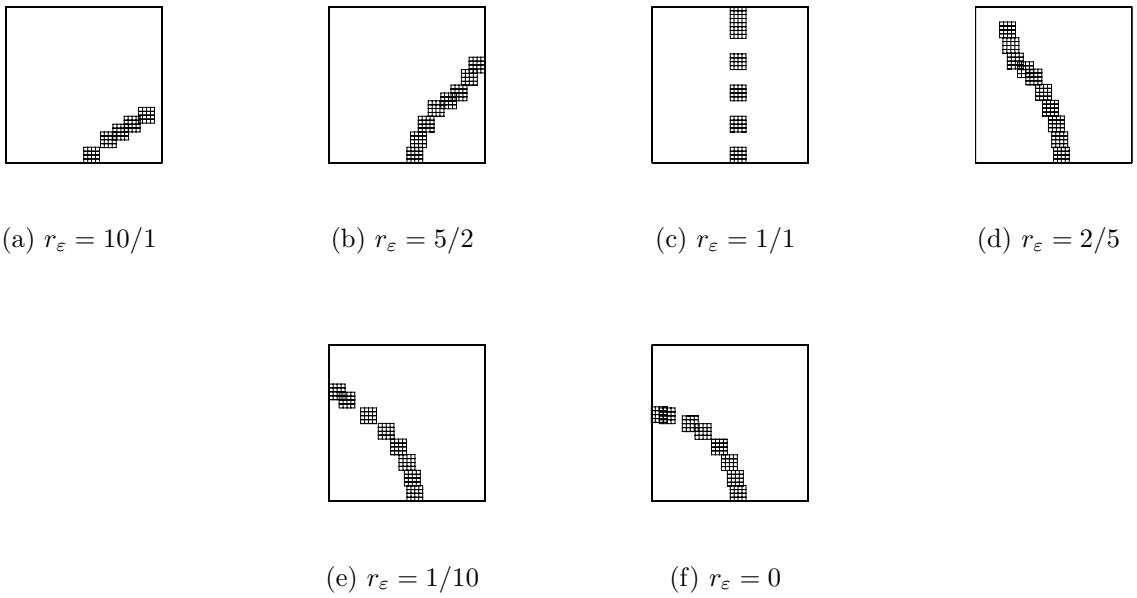

(a) $r_\varepsilon = 10/1$ (b) $r_\varepsilon = 5/2$ (c) $r_\varepsilon = 1/1$ (d) $r_\varepsilon = 2/5$

(e) $r_\varepsilon = 1/10$ (f) $r_\varepsilon = 0$

Figure 19: Motion of the block in the case of polar orthotropy on the plane. Varying adhesion tensor parameters: $r_\varepsilon = \varepsilon_\varphi/\varepsilon_r = 10/1,\ 5/2,\ 1,\ 2/5,\ 1/10,\ 0$; isotropic friction tensor parameters: $\mu_1 = \mu_2 = 0.2$. Loading by prescribed vertical displacement w and incremental y-displacement Δu.

with $g_\varepsilon = \varepsilon_1 R^2 + \varepsilon_2 \left(\dfrac{H}{2\pi}\right)^2$.

The adhesion tensor parameters are varying according to Table 2.

Case	Adhesion tensor	Ratio r_ε	Resulting distance h
1	$\varepsilon_1 = 0.0$ $\varepsilon_2 = 10.0$	0.0	$1.000\,H$
2	$\varepsilon_1 = 5.0$ $\varepsilon_2 = 10.0$	1/2	$0.742\,H$
3	$\varepsilon_1 = 7.5$ $\varepsilon_2 = 10.0$	3/4	$0.430\,H$
4	$\varepsilon_1 = 10.0$ $\varepsilon_2 = 10.0$	1.0 geom. isotropy	$0.000\,H$
5	$\varepsilon_1 = 10.0$ $\varepsilon_2 = 5.0$	2/1	$-0.487\,H$
6	$\varepsilon_1 = 10.0$ $\varepsilon_2 = 7.5$	4/3	$-2.758\,H$
7	$\varepsilon_1 = 10.0$ $\varepsilon_2 = 0.0$	∞	$-31.98\,H = \hat{H}$

Table 2: Rotation of a bolt. Variation of parameters of the adhesion tensor. Resulting distance of a longitudinal motion h after rotation of a bolt by 360^o.

The results of the analyses are depicted in Fig. 21 showing the computed longitudinal motion of the bolt along the OZ-axis vs. the applied rotation angle. The resulting distance of a longitudinal motion h after the rotation of a bolt by 360^o is also presented in Table 2. Case

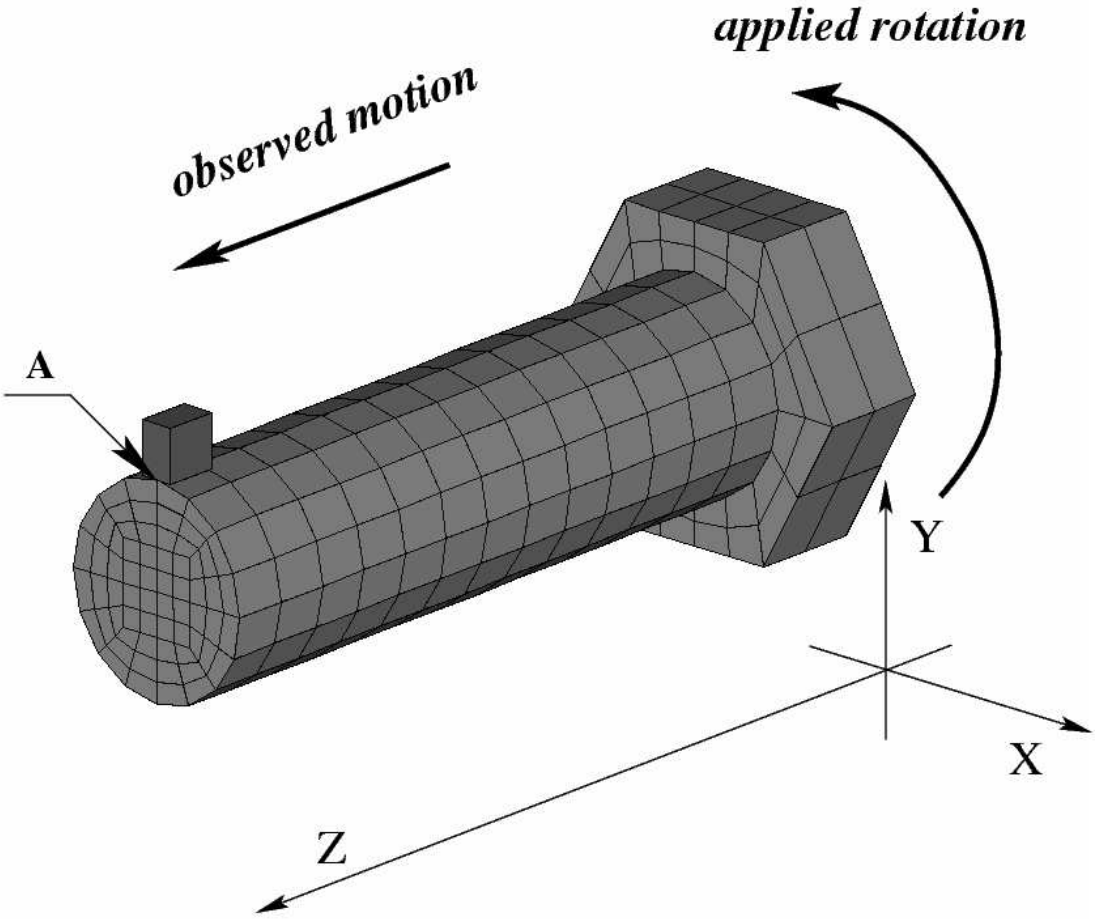

Figure 20: Finite element model of a bolt connection. Outer surface is rigid and is illustrated with one element only.

(1) with ratio $r_\varepsilon = 0$ leads to a pure forward motion according to the motion along the main spiral line, see Part 1. The bolt moves forward at the distance H while the bolt is rotating at the full angle 360^o. The geometrically isotropic case (4) does not lead to any longitudinal motion. For ratios $r_\varepsilon > 1$ a backward motion is obtained. Finally, the case (7) with ratio $r_\varepsilon = \infty$ (not shown in Fig. 21) leads to a motion along the orthogonal spiral, i.e. the bolt moves backwards at the distance $\hat{H} = \dfrac{(2\pi R)^2}{H}$, see **Remark 4** Sect. 3 in Part 1.

Remark. This example is only chosen to illustrate the possibility to describe machined surface from a kinematical point of view. The applicability of the proposed model to stress analysis of the bolt connection requires, certainly, a more sophisticated analysis.

Remark. The presented technique has been implemented into the FEAP-MeKa code [13]. The unsymmetric solver is based on a standard **LU**-decomposition combined with an iterative Newton scheme.

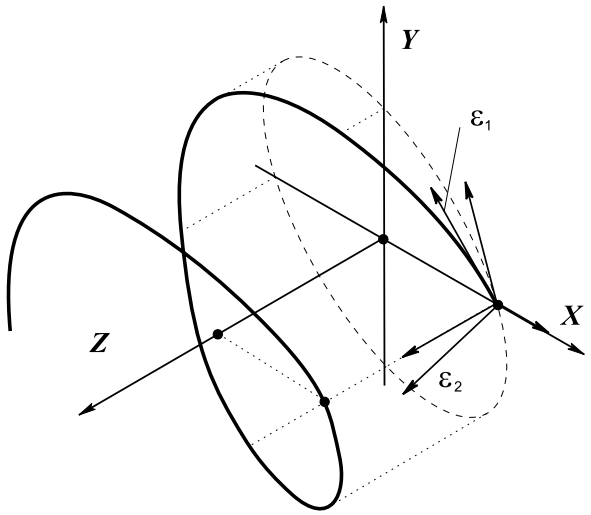

(a)

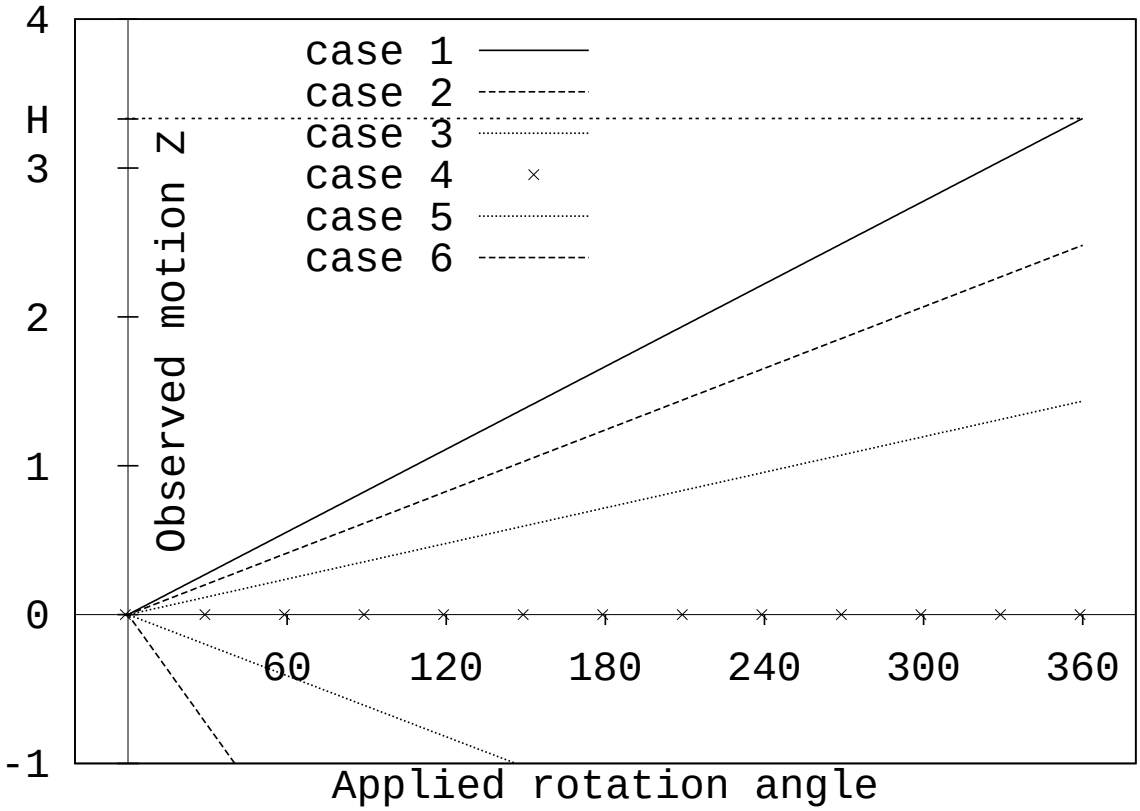

(b)

Figure 21: a) Spiral orthotropy on a cylinder. b) Observed longitudinal motion vs. applied rotation. Variation of ratio $r_\varepsilon = \varepsilon_1/\varepsilon_2$. Loading cases according to Table 2.

5 Conclusions

In the current part the numerical analysis of the model of contact interfaces including anisotropy for adhesion and friction developed in Part 1 is presented. The linearization necessary for the

numerical iterative solution is considered in a covariant form in the metrics of a tangent plane. The covariant form makes the application of the derived scheme to contact problems with arbitrary curved surfaces possible. A numerical implementation into finite element codes is also considered leading to a family of contact elements based on a) a point-to-analytical approach for both linear and curvilinear approximations of the contact body and b) a node-to-segment approach. In addition, a rheological model based on a simple mechanical interpretation of the model is discussed.

The proposed model for contact interfaces is analyzed for constant orthotropy on a plane, for polar orthotropy on a plane and for spiral orthotropy on a cylinder. The reliability of the numerical results is controlled by checking the convergence with increasing the adhesion parameters and by remeshing. A classification of orthotropy based on the ratio of eigenvalues for the corresponding orthotropic tensor is proposed and the kinematical effects for the classified cases are numerically investigated. In particular, as a specific case of complex anisotropy the geometrically isotropic kinematic behavior of the contact bodies can be found despite the presence of both, anisotropy for adhesion and friction. The possibility of modeling machined surfaces with the help of the adhesion tensor is shown by numerical examples for polar orthotropy and for the model of a bolt connection.

The presented approach shows an algorithmic inclusion in covariant form only for linear elastic adhesion and for an associated Coloumb's friction law. Any combination of elastic, viscoelastic or nonlinear laws for the adhesion region together with non-associative or associative friction laws can be derived in straightforward covariant manner based on the metrics of the contact surfaces.

6 Acknowledgments

We thank the DFG for the support given by grant SCHW 307/18-2. We also thank Prof. Vielsack, Institut für Mechanik, Universität Karlsruhe for many creative discussions, in particular, concerning the rheological model for the contact interfaces including adhesion and friction.

A APPENDIX. Recovering a circular motion for polar orthotropy.

A family of curves in the case of polar orthotropy with the parameter $\varepsilon_\varphi = 0$ for the problem considered in Sect. 4.3 is a family of circles.

In order to prove this statement we consider the equilibrium equations for the quasi-statical sliding of a block, see Fig. 18, Sect. 4.3.

$$\begin{aligned} T_1 &= 0 \\ T_2 + F &= 0. \end{aligned} \tag{39}$$

Here a force F is associated with applied displacements along OY axis and T_1, T_2 are components of a sliding force $\mathbf{T}^{sl}$ defined in eqn. (10). Following the incremental displacement loading process and the definition of the sliding force via the trial force, see also eqn. (12) we can write:

$$\mathbf{T}^{sl} = -|N|\frac{\mathbf{BFB}}{\Psi}\left\{ \begin{array}{c} \Delta u \\ \Delta v \end{array} \right\}, \tag{40}$$

where Δu is a prescribed displacement component and Δv is a computed component from the equilibrium equation. Then from the first equilibrium equation (39) we obtain:

$$\mathbf{BFB}_{11}\Delta u + \mathbf{BFB}_{12}\Delta v = 0. \tag{41}$$

The limit of the ratio of the displacement increments when Δu goes to zero leads to the exact definition of the derivative:

$$\lim_{\Delta u \to 0} \frac{\Delta v}{\Delta u} = y' = -\frac{\mathbf{BFB}_{11}}{\mathbf{BFB}_{12}}. \tag{42}$$

Now, we specify the particular case with an isotropic friction tensor $\mathbf{F} = \mathbf{E}/\mu^2$ and $\varepsilon_\varphi = 0$ in the adhesion tensor $\mathbf{B}$ in eqn. (37) leading to

$$\mathbf{B} = -\frac{\varepsilon_r}{x^2 + y^2}\left[\begin{array}{cc} x^2 & xy \\ xy & y^2 \end{array} \right]. \tag{43}$$

Inserting the corresponding components from eqn. (43) into eqn. (42) we obtain an ordinary differential equation (ODE) describing a family of curves (trajectory of the ODE):

$$y' = -\frac{x}{y}. \tag{44}$$

The integration of this differential equation leads to

$$y^2 + x^2 = const, \tag{45}$$

which describes a family of circles.

References

[1] Alart, P., Heege, A. Consistent tangent matrices of curved contact operators involving anisotropic friction. *Revue europeenne des elements finis.* **4** (1995) 183–207.

[2] Buczkowski, R., Kleiber, M. Elasto-plastic interface model for 3D-frictional orthotropic contact problems. *International Journal for Numerical Methods in Engineering.* **40** (1997) 599–619.

[3] Buczkowski, R., Kleiber, M. Statistical model of strongly anisotropic rough surfaces for finite element contact analysis. *International Journal for Numerical Methods in Engineering.* **49** (2000) 1169–1189.

[4] Harnau, M., Konyukhov, A., Schweizerhof, K. Algorithmic aspects in large deformation contact analysis using 'Solid-Shell' elements. *Computers and Structures.* **83** (2005) 1804–1823.

[5] Hjiaj, M., Feng, Z.-Q., de Saxce, G., Mroz, Z. Three-dimensional finite element computations for frictional contact problems with non-associated sliding rule. *International Journal for Numerical Methods in Engineering.* **60** (2004) 2045–2076.

[6] Johnson, K. L. *Contact mechanics* (Cambridge: Cambridge Univ. Press, 2001).

[7] Jones, R.E., Papadopoulos, P. Simulating anisotropic frictional response using smoothly interpolated traction fields. *Computer Methods in Applied Mechanics and Engineering.* **195** (2006) 588–613.

[8] Konyukhov A., Schweizerhof K. Contact formulation via a velocity description allowing efficiency improvements in frictionless contact analysis. *Computational Mechanics.* **33** (2004) 165–173.

[9] Konyukhov A., Schweizerhof K. Covariant description for frictional contact problems. *Computational Mechanics.* **35** (2005) 190–213.

[10] Konyukhov A., Schweizerhof K. Covariant description of contact interfaces considering anisotropy for adhesion and friction. Part 1. Formulation and analysis of the computational model. *Computer Methods in Applied Mechanics and Engineering.* (submitted).

[11] Montmitonnet, P., Hasquin A., Implementation of an anisotropic friction law in a 3D finite element model of hot rolling. *Simulation of Materials Processing: Theory, Methods and Applications.* NUMIFORM'95, edited by S.-F. Shen and P. Dowson. Balkema, Rotterdam (1995) 301–306.

[12] Simo, J.C., Hughes, T.J.R. *Elastoplasticity and Viscoplasticity: computational aspects*, Springer-Verlag: Berlin, (1992).

[13] Taylor R.L. FEAP – A Finite Element Analysis Program. University of California at Berkeley, Berkeley. Schweizerhof, K. and Coworkers, FEAP - Mechanik - Karlsruhe, Institut für Mechanik, Universität Karlsruhe. (1987).

[14] Zmitrowicz, A. An equation of anisotropic friction with sliding path curvature effects. *International Journal of Solids and Structures.* **36** (1999) 2825–2848.

[15] Zmitrowicz, A. Illustrative examples of anisotropic friction with sliding path curvature effects. *International Journal of Solids and Structures.* **36** (1999) 2849–2863.

[16] Zmitrowicz, A. Models of kinematics dependent anisotropic and heterogenous friction. *International Journal of Solids and Structures.* **195** (2006) 588–613.

[17] Zhang, H. W., He, S. Y., Li, X.S., Wriggers, P. A new algorithm for the numerical solution of 3D elastoplastic contact problems with orthotropical friction law. *Computational Mechanics.* **34** (2004) 1–14.

Contents